Hybrid Structure Design of Lightweight Robotic Arms Based on Carbon Fiber Reinforced Plastic and Aluminum Alloy

HAIBIN YIN, JING LIU, AND FENG YANG

Key Laboratory of Hubei Province for Digital Manufacture, School of Mechanical and Electronic Engineering, Wuhan University of Technology, Wuhan 430070, China

Corresponding author: Haibin Yin (chinaliuyin@whut.edu.cn)

ABSTRACT Some light materials, such as hollow sphere composite (HSC), carbon fiber reinforced plastic (CFRP), and aluminum alloy (AA), are currently used in the design of lightweight robotic arms. However, the high cost limit the use of HSC, the CFRP has a relatively low cost but poor processing property, and the AA has good processing property but relatively high density. To make up respective shortcomings, this study focuses on the design issues of lightweight robotic arms by using two kinds of materials. Based on the CFRP and AA, a hybrid structure design approach is proposed to minimize the total mass of the lightweight robotic arms with CFRP/AA hybrid structure. To accomplish the objective, structural dimensions and layer parameters in hybrid structures are parameterized as design variables subject to the strength, stiffness, and dynamic constraints. Moreover, the bonding strength of the interaction surfaces between CFRP and AA parts is also considered on the basis of the cohesive zone model (CZM). In optimization design, the ABAQUS and elitist non-dominated sorting genetic algorithm (NSGA-II) in modeFRONTIER utilizing the Python script are respectively employed for the structural analyses and iteration calculation. Finally, a design example and an experimental prototype are provided to validate the proposed method and compare with the previous AA prototype in mass with a reduction of 24.32%.

INDEX TERMS Lightweight robotic arm, hybrid structure, optimization design, carbon fiber reinforced plastic, aluminum alloy.

I. INTRODUCTION

Under the requirements of energy-efficiency and productivity, lightweight robotic arms are increasingly employed in the fields of industry, agriculture, service, and space exploration. The lightweight robotic arm denotes that it is required to reduce the weight of the arms satisfying specific conditions. To realize the lightweight design of robotic arms, there are three ways: drivetrain design for high torque density, structure optimization for fewer materials and use of light materials.

Drivetrains used as actuators in the robotic arm account for a large proportion of the total mass, so they have a lot of potential for the improvement of torque density of these actuators. Smart materials, which are popularly used as actuator of soft robot, possess high torque density, such as dielectric elastomeric actuators (DEA) [1], electro active

polymer (EAP) [2], and shape memory alloy (SMA) [3]. However, these artificial muscles, which can contribute lightweight or adaptability, produce poor dynamic performance and positioning accuracy, and some drawbacks limiting their utility in specific cases. In the need of good dynamic performance and positioning accuracy of the lightweight robotic arm, traditional drivetrains are still the most common for lightweight design by increasing its torque density. Fujishima *et al.* introduced an optimization method to quickly design a permanent synchronous motor for high torque density [4]. Jing *et al.* proposed a structural design method for brushless DC motor in robotic joint [5]. Sulaiman *et al.* firstly studied the torque of a dual excitation switch-flux (DESF) motor, and then adopted a deterministic approach to optimize DESF motor's parameters and improve its torque density for target performances [6]. However, these studies were implemented to increase the torque density of motors, but disregarding

---

The associate editor coordinating the review of this manuscript and approving it for publication was Huaqing Li.

the combination with gears or structure of robotic arm. Pettersson and Ölvander proposed a drivetrain optimization for finding the trade-offs between lifetime, properties and cost of industrial robots [7]. Zhou et al. presented an integrated optimization method to design a lightweight anthropomorphic arm, which is optimized based on the drivetrains selected from commercial catalog [8]. Nevertheless, the growth on the torque density of drivetrains is limited under the current technology conditions, and more the lightweight optimization of drivetrain is dependent on the structural parameters. Therefore, the structural optimization is the main way for lightweight robotic arms when the types or technologies of drivetrains are determined.

Structural optimization can reduce the unwanted material subject to the specific conditions. Shiakolas et al. discussed optimum robot design to minimize the torque required for the motion subject to defection and physical constraints with the design variables being the structural dimensions [9]. Kim et al. presented a topology optimization method for the design of lightweight serial robots and performed the topology optimization of a robot structure by dividing the problem into part-level optimization [10]. Structural optimization could reduce the weight of structure, but it could also lead the system to be prone to flexible vibration. Hence, the dynamic compensation for stiffness is required to contribute the grade of lightweight by means of feedback control [11] and trajectory planning [12]. Fonseca and Bainum utilized semi-analytical approach to compute the sensitivity with respect to design parameters, and performed an integrated structural/control optimization of a large space structure with a robot arm for obtaining the minimum weight and optimal dynamic performance [13]. Lee et al. optimized the kinematic variables of a welding robot for considering a mass reduction, and the desired trajectory of the welding robot was obtained through two steps of coarse and fine searching [14]. Both the structural optimization and dynamic compensation for stiffness aim at enhancing the stiffness-to-mass ratio from macro-scale level. While light materials with larger stiffness-to-mass ratio could attain lighter structure from micro-scale level.

With development of material technique, there have been serval light materials with high stiffness and low density. Cheng et al. designed a fully plastic micro robot (FPMR) through the combination of the Cross-linked liquid-crystalline polymers and polyethylene films [15]. Similarly, flexible plastic was applied into the fabrication of underwater robot (UWR) to reduce its weight and the force generated by the differential pressure between inside and outside of the robot [16]. The plastic materials used in both the FPMR and UWR have high stiffness-to-mass ratio, but its absolute strength and stiffness are low. Hagenah et al. designed and manufactured the flanges of the robotic arms with titanium and joint housing with nanocrystalline aluminum alloy, which can attain lighter structure than the conventional casting counterpart [17]. Baumeister and Klaeger reported the application of hollow-sphere-composite

(HSC) [18] and used it to fabricate the SCARA robot arm, which is demonstrated with good static and dynamic properties compared with AA arm [19]. These abovementioned materials have high stiffness-to-mass ratio and absolute strength, but high cost results in a barrier for wide usage in robotic arms. Some notable lightweight robotic arms, such as UR [20] and KUKA [21], were made of low-cost AA materials. In addition, Fiber reinforced plastic (FRP) possess not only relative low cost but also the high stiffness-to-mass ratio, so it is widely used in the design of lightweight structure. Liao et al. analyzed the optimal geometry and material fabrication parameters of lightweight arm with FRP [22]. Lee et al. introduced two kinds of robotic wrist blocks with carbon FRP (CFRP) and glass FRP (GFRP) to compare their stiffness [23]. Yoo et al. designed a subsea walking robot with CFRP to protect the robot from corroding and reduce its weight in contrast with the conventional metallic robot [24]. CFRP is a kind of popular material with good properties and widely used in lightweight structures, however, the CFRP materials are unsuitably used in the structure, which is complex part required connect in multi-body system, due to its poor processing property.

To avoid the fiber damage caused by machining, the complex pieces connecting with other parts could be fabricated by metal materials with good processing property and bonded with the CFRP structure. Mutasher et al. studied and fabricated a hybrid shaft by winding CFRP onto an AA tube with different winding angles and numbers of layers, and denoted that the hybrid shaft has a better bending fatigue property when the fiber placement with 45° [25]. Feng et al. investigated CFRP/AA hybrid tubes by using compression experiments and a theoretical analysis, where formulas describing the compressive bearing capacity with and without local buckling before yielding are proposed for the hybrid tubes [26]. The hybrid tube is a single component with simple shape and the corresponding researches disregarded the adhesive strength between both the parts with different materials, while the complex part used in multi-body structure is required to consider the adhesion strength. The cohesive zone model (CZM) is generally used in the analysis of the failure characteristics in the hybrid structure [27]. Ribeiro et al. used CZM to perform a detailed stress analysis that enables the comparison between different planes in the adhesive joint and values of overlap length in the hybrid structure [28]. Jeon et al. proposed a design of CFRP/AA hybrid upper arm for the pantograph of high-speed trains in consideration of the failure of adhesion layer at high temperature and its mechanical performance [29]. These investigations involving the geometry parameters, layer numbers as well as the adhesive strength in the hybrid structure are useful reference in the design of lightweight structure. JACO is a typical lightweight robotic arm with CFRP/AA hybrid structure [30], but the closed CFRP shell, in which its AA actuator is completely embedded, results in difficulty of dispersing heat.
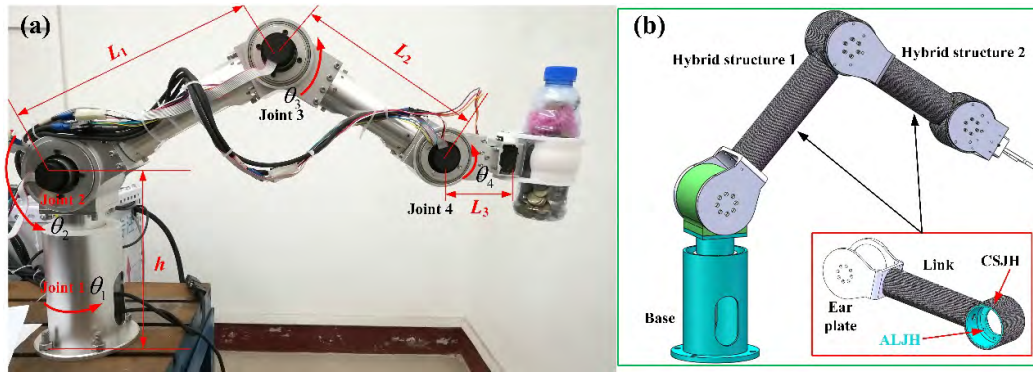
FIGURE 1. (a) Prototype of robotic arm made of AA and (b) model of robotic arm based on CFRP/AA.

This study extends the hybrid structure method in the previous design of the 4-DOF robotic arm with AA material [31] to improve its lightweight level and heat dissipation. The hybrid structure design is presented as an optimization problem, which minimizes the weight of robotic arm subject to the constraints conditions on structural strength, stiffness and dynamic performance, as well as adhesive strength between AA and CFRP components. In the optimization, the structural parameters of AA parts and the stacking sequences and layer numbers of CFRP components are defined as design variables. The hybrid structures of robotic arm are simultaneously optimized on the basis of NSGA-II instead of multi-level optimization algorithm, so this design could obtain a global optimum solution for the lightweight robotic arm. Finally, a CFRP/AA experimental prototype is fabricated, and then series of experiments on the lightweight feature and dynamic characteristics of the hybrid structure prototype is measured to compare with the AA prototype and validate the optimization method.

II. PROBLEM STATEMENT AND DESIGN CONDITIONS

In general, AA is a preferred material for lightweight robotic arms considering the cost and processing. Figure 1(a) shows an AA prototype of the 4-DOF robotic arm, which was developed for service tasks in mobile robot based on the previous research [31]. However, the AA prototype was implemented as a conceptual design with holes and slots to reduce the weight of robotic arms, moreover the AA material constituting the prototype have provided low damping ratio and limited lightweight design. Hence, a lighter material with higher damping ratio and a streamline design with round shape are required. To realize this target, composite material CFRP, which is characterized by low density, high strength and damping ratio, is an ideal alternative. CFRP is commonly used as the structural material to build monolithic components because it is not suitable to use the machining process for bolt and assembly connects. However, the robotic arms are typical multibody structures and the connecting part of each component at joint is required to use machining process. Therefore, a hybrid structure integrating the links made of CFRP and the connecting part manufactured from AA is presented to design the lightweight robotic arm.
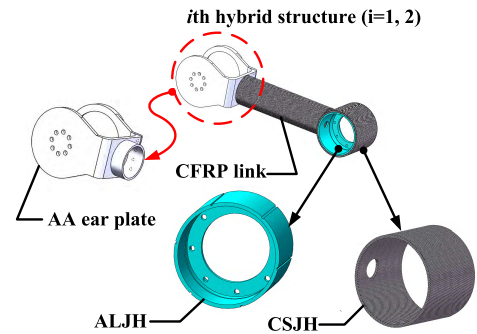
A. PROBLEM STATEMENT

Figure 1(b) depicts the model of robotic arm with hybrid structures, which consist of the connecting parts and links. The connecting parts include the ear plates and lining of joint housing made of AA (ALJH), which are characterized by complex geometrical shapes with assembly and connecting holes. The CFRP links are built as a monolithic component with the shell of joint housing made of CFRP (CSJH). The hybrid structure made of both the AA and CFRP materials show complex shape and anisotropy based on machining, bonding and forming processes, so the lightweight design is a challenging task. To obtain the optimal hybrid structure, the whole robotic arm with CFRP/AA hybrid structures is modeled and analyzed in ABAQUS, where the hybrid structures are parameterized to optimize the robotic arm in consideration of the objective function as well as the working and constraints conditions. In this optimization problem, the main parameters of links and joint housing in the hybrid structures are defined as the design variables, and the corresponding constraints conditions are presented to ensure the validity of optimal results.

B. PRECONDITION OF DESIGN

The optimization design of the lightweight robotic arm with hybrid structures is conducted on the basis of the AA prototype and only the upper arm and forearm are replaced with CFRP/AA hybrid structures. Thus, several structural parameters are used as the same values with the AA prototype, for example, the lengths of links and height of base are used as $L_1 = 319$ mm, $L_2 = 251$ mm, $L_3 = 130$ mm, $h = 250$ mm as shown in Fig. 1(a). Moreover, the lengths of the upper arm and forearm (L_1 and L_2) are determined by considering global condition index (GCI) [32] parameter as 0.3125 to obtain the optimal workspace [31]. In addition to these structural parameters, the robotic arm with hybrid structures is actuated by these drivetrains, which are composed of the same Maxon motors and XBHY harmonic gears used in the AA prototype as listed in Table 1. The AA prototype was designed by considering the specific task conditions, and the robotic arm with CFRP/AA hybrid structure is optimized on the basis of the same task conditions, which are termed as the load and trajectories.
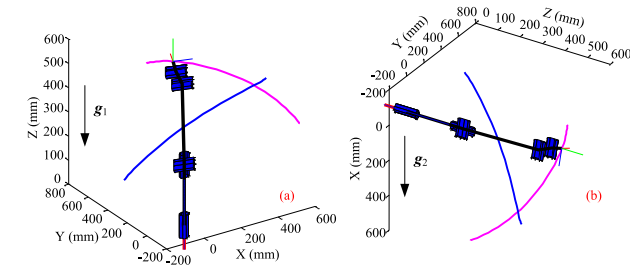
TABLE 1. Motors and harmonic gears used in the four joints.

Joint number	Harmonic gear	Maxon motor	Rated torque (Nm)	Weight (kg)
1	HBHY-17-120	ECI-40	21.341	1.190
2	HBHY-17-120	ECI-40	21.341	1.190
3	HBHY-17-120	EC-45	11.674	0.830
4	HBHY-14-120	EC-45	2.462	0.607

FIGURE 2. Two types of trajectories in (a) ground and (b) wall installations.

TABLE 2. Installation types and trajectories.

Installation type	Starting position q_s	Ending position q_e	t_p(s)
Ground installation	$[\pi/2, \pi/3, -\pi/2, \pi/2]$	$[0, -\pi/12, -\pi/6, \pi/3]$	3
	$[0, \pi/2, -\pi/2, 0]$	$[\pi/2, \pi/6, -\pi/3, \pi/6]$	3
Wall installation	$[\pi/2, \pi/3, -\pi/2, \pi/2]$	$[0, -\pi/12, -\pi/6, \pi/3]$	3
	$[0, \pi/2, -\pi/2, 0]$	$[\pi/2, \pi/6, -\pi/3, \pi/6]$	3

The kinematic and dynamic simulations of the robotic arm are analyzed by considering a group of trajectories. As shown in Fig. 2, the robotic arm moves along two types of trajectories in each installation, which is divided by gravity vectors $g_1 = [0, 0, -1]$ and $g_2 = [1, 0, 0]$. Therefore, the robotic arm is conducted in four motions totally, and these motions are described with the starting and ending positions as listed in Table 2. Using polynomial interpolation, these trajectories are represented by:

$$q_j(t) = \left\{ a_0 + a_1 t + a_2 t^2 + a_3 t^3 + a_4 t^4 + a_5 t^5 \right\}_j,$$
$$j = 1, 2, 3, 4, \tag{1}$$

where the six coefficients could be determined by using the values of positions, velocities and accelerations at the starting time $t_1 = 0$ and ending time $t_2 = 3$ s.

In addition, the target payload m_e, which is a mass point, is given as 2 kg in this study.

C. DESCRIPTIONS OF HYBRID STRUCTURE

Figure 3 shows the principal model of the *i*th hybrid structure ($i = 1, 2$), which includes the CFRP link and the CFRP shell of joint housing (CSJH), as well as the AA ear plate

FIGURE 3. Principal model of the *i*th hybrid structure ($i = 1, 2$).

and the AA lining of joint housing (ALJH). The both types of parts are connected by bonding or packing prepreg process. To fasten the connection, The ALJH was fabricated with some technology grooves before packing and forming with CFRP, and the AA ear plate was bonded with the CFRP link by using a bonding layer.

III. OPTIMIZATION PROBLEM AND METHOD

Based on the abovementioned design conditions and descriptions of hybrid structure, a hybrid structure design of the lightweight robotic arm are proposed in this section. It is an optimization problem aiming at hybrid structures and the optimization process is implemented in the integration platform including ABAQUS and modeFRONTIER.
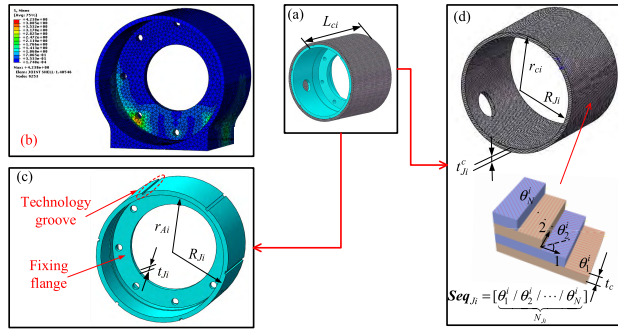
A. DESIGN VARIABLES

In the optimization process, the hybrid structures are optimized by considering the design variables of the joint housings and links.

1) DESIGN VARIABLES OF JOINT HOUSING

As shown in Fig. 4(a), the *i*th joint housing is a part of the *i*th hybrid structure. To connect with the CFRP link and install the drivetrain, the joint housing is designed into two parts: ALJH and CSJH as shown in Figs. 4(c) and (d). The CSJH part is integrated with the CFRP link by forming in a steel mold and also wrapped on the surface of the ALJH part. Thus, the design variables of the joint housing consisting of the both ALJH and CSJH parts are described as these corresponding parameters of the ALJH and CSJH parts.

Using FEA in ABAQUS, the stress distribution pattern of the second joint housing in AA prototype is obtained as shown in Fig. 4(b). We can summarize that the maximum stress occurs around the bolt holes and transitional area on the fixing flange. Consequently, the thickness t_{Ji} of the fixing flange is a significant factor to influence the strength of joint housing and is selected as one design variable of joint housing as shown in Fig. 4(c). In addition, the external radius R_{Ji} of the ALJH part is optimized to reduce the weight of joint housing. In the optimization design, the inside radius r_{Ai} and the axial length L_{ci} of the ALJH part are fixed to match the structural

FIGURE 4. (a) Model of joint housing, (b) stress pattern of joint housing in AA prototype, (c) design variables of ALJH and (d) design variables of CSJH.

FIGURE 5. (a) Hybrid structure model and (b) design variables of the CFRP link.

dimensions of drivetrains, which are given and used in the AA prototype. As a result, the design variables of the ALJH parts are described as:

$$H_J^A = \left(H_{J1}^A, H_{J2}^A\right) = \left(R_{J1}, t_{J_1}, R_{J_2}, t_{J_2}\right), \qquad (2)$$

where H_J^A represents all design variables of the ALJH parts, H_{J1}^A and H_{J2}^A denote the design variables of the ALJH parts in the first and second hybrid structures. Superscript A represents AA component.
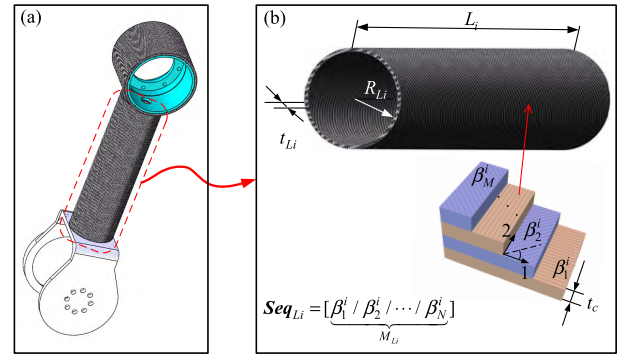
Figure 4(d) depicts the CSJH part, its inside radius R_{Ji} is same with the external radius of the ALJH part due to the connection relation. Additionally, the thickness t_{Ji}^c of the CSJH part is related with the each ply thickness t_c and the ply number N_{Ji}, and the each ply thickness t_c is a fixed value that is dependent on the dimension of prepreg. Hence, the ply number N_{Ji} that determines the thickness of the CSJH part is taken into account as one design variable. Moreover, it can be observed that θ_N^i is the Nth ply orientations in the ith CSJH part, these ply orientations are termed as stacking sequence or a vector Seq_{Ji}. To balance the stack and obtain excellent mechanics properties, the ply orientations in stacking sequence are designed symmetrically, so the actual ply number are double the independent ply number N_{Ji}. Since the stacking sequence have an impact on the integral stiffness and frequency of robotic arms, it is used as design variables and expressed as $Seq_{Ji} = \left[\theta_1^i/\theta_2^i/\ldots/\theta_N^i\right]s$, where each element is a specific ply angle and selected from the set {-45°, 0, 45°, 90°} due to the limitation on raw materials and cost. The design variables of the CSJH parts are described as:

$$H_J^C = \left(H_{J1}^C, H_{J2}^C\right) = \left(N_{J1}, Seq_{J1}, N_{J2}, Seq_{J2}\right), \qquad (3)$$

where H_J^C represents all design variables of the CSJH parts, H_{J1}^C and H_{J2}^C denote the design variables of the CSJH parts in the first and second hybrid structures. Superscript C represents CFRP component.

As a result, the design variables of joint housings are defined as a vector H_J, which can be represented by:

$$\begin{aligned} H_J &= (H_{J1}, H_{J2}) \\ &= \left(N_{J1}, Seq_{J1}, R_{J1}, t_{J1}, N_{J2}, Seq_{J2}, R_{J2}, t_{J2}\right), \quad (4) \end{aligned}$$

where H_{J1} and H_{J2} denotes the design variables of joint housings in the first and second hybrid structures, respectively.

2) DESIGN VARIABLES OF LINKS

As shown in Fig. 5(a), the CFRP link is a cylindrical shell in the ith ($i = 1, 2$) hybrid structure. To compare the kinematics performance of the proposed robotic arm with the AA prototype, the lengths L_i of the CFRP links in the hybrid structures are the same values as the AA counterpart determined in the previous optimization based on GCI [32]. Similarly, the inner radius R_{Li} of cylindrical link is set as given value for connection with the ear plate. Regarding the weight of the CFRP link, the thickness t_{Li} of cylindrical link, which is related to the ply number M_{Li} and each ply thickness t_c, should be limited. Because the ply thickness is constant due to the use of prepreg, the thickness of cylindrical link is only dependent on the ply number M_{Li}.

Consequently, the design variables of the ith CFRP link are described as ply number M_{Li} and stacking sequence $Seq_{Li} = \left[\beta_1^i/\beta_2^i/\ldots/\beta_M^i\right]_s$, where the symbol β_M^i denotes the Mth ply angle in the CFRP link of the ith hybrid structure, and the ply angles are limited to select from the specific range {−45°, 0, 45°, 90°}. All design variables of the both CFRP links can be represented by:

$$H_L = (H_{L1}, H_{L2}) = \left(M_{L1}, Seq_{L1}, M_{L2}, Seq_{L2}\right), \qquad (5)$$

where H_{L1} and H_{L2} denote the design variables of the CFRP links in the first and second hybrid structures, respectively.

In addition to the design variables of CFRP links, a characteristic parameter related to the thickness and length of link, is defined as:

$$\lambda = t_{Li}/L_i, i = 1, 2, \qquad (6)$$

If the value of the characteristic parameter λ is less than 0.1, the CFRP links can be discretized into shell element in finite element method to improve calculation efficiency.

3) DESIGN VARIABLES OF HYBRID STRUCTURES

Consequently, the design variables of the hybrid structures in the robotic arm are briefly expressed as:

$$\begin{aligned}
\mathbf{X} &= (\mathbf{X}_1, \mathbf{X}_2) \\
&= \begin{pmatrix} M_{L1}, \boldsymbol{Seq}_{L1}, N_{J1}, \boldsymbol{Seq}_{J1}, R_{J1}, t_{J1}, M_{L2}, \\ \boldsymbol{Seq}_{L2}, N_{J2}, \boldsymbol{Seq}_{J2}, R_{J2}, t_{J2} \end{pmatrix},
\end{aligned} \tag{7}$$

where X, X_1 and X_2 are the design variables of the both hybrid structures, design variables of the first and second hybrid structure, respectively.

These design variables related to the kinematics and dynamic behavior of robot are renewed in the entire design process to obtain the optimal objective and meet the corresponding constraint conditions.

B. CONSTRAINTS CONDITIONS

In the lightweight optimization of robotic arm with hybrid structures, these constraints on strength, stiffness, and bonding damage are supposed to be considered to validate the computations.

1) CONSTRAINTS ON STRENGTH

The hybrid structures of robotic arm are composed of AA parts and CFRP components; hence the optimization need consider the corresponding strength conditions for different material parts.

For AA parts, the Von-Mises equivalent stress of the ALJH and ear plate are mainly considered to satisfy the constraints on structural strength and represented by:

$$S_1 \sigma_A (\mathbf{X}) \leq \sigma_s, \tag{8}$$

where X is the design variables of hybrid structures, and σ_A and σ_s denote the maximum Von-Mises equivalent stress of AA parts and the yield strength of AA material. The symbol S_1 is the structural safety coefficient.

These constraints on structural strength are evaluated through the static structural analysis in ABAQUS and imported into modeFRONTIER to optimize the structural parameters.

For CFRP parts, the internal stresses are simulated according to the failure criteria, which is different from isotropic AA material. Comparing with the maximum stress and maximum strain criterions, the Tsai–Wu criterion [33] presents a concise analytical expression in consideration of the strong coupling effects among the stress components. To validate strength analysis for CFRP parts under the action of load, the Tsai–Wu failure criterion is used in strength analysis and described as:

$$\begin{aligned}
C_v &= F_{11} \left[\sigma_1(\mathbf{X})\right]^2 + 2F_{12}\sigma_1(\mathbf{X})\sigma_2(\mathbf{X}) + F_{22} \left[\sigma_2(\mathbf{X})\right]^2 \\
&+ F_{66} \left[\tau_{12}(\mathbf{X})\right]^2 + F_1\sigma_1(\mathbf{X}) + F_2\sigma_2(\mathbf{X}) < C_{v\max},
\end{aligned} \tag{9}$$

where σ_1 and σ_2 are the normal stress related to the fiber orientation and transverse direction, and τ_{12} is shear stress; C_v and $C_{v\max}$ are the Tsai-Wu failure index and its maximum permissible value; the coefficients are described as:

$$F_{11} = 1 \big/ (X_c X_t), \quad F_{12} = 1 \big/ (X_c X_t Y_c Y)^{1/2},$$

$$F_{22} = 1 \big/ (Y_c Y_t), \quad F_{66} = 1 \big/ S^2,$$
$$F_1 = (X_c - X_t) \big/ (X_c X_t), \quad F_2 = (Y_c - Y_t) \big/ (Y_c Y_t), \tag{10}$$

where X_c and X_t represent the compression and tension failure stress in fiber orientation, Y_c and Y_t denote compression and tension failure stress in transverse direction, S is the shear failure stress.

When the value of C_v is not less than 1, the CFRP structure is termed as failure. Until the value of C_v is smaller than 1, the CFRP parts in the robotic arm are feasible.

2) CONSTRAINTS ON STIFFNESS

The robotic arm yields the deformation when its stiffness is insufficient due to the lightweight design. Therefore, the constraints on stiffness reflected by the deformation and frequency are required to consider in optimization.

In the design, the maximum value of deformation at the end-effector of the robotic arm is calculated and need meet the following conditions as:

$$S_2 u (\mathbf{X})_{\max} \leq \mathbf{d}_a, \tag{11}$$

where $u(\mathbf{X})_{\max}$ is the maximum values of deformation at end-effector of the robotic arm in three-dimension coordinates, d_a is the allowable values of deformation at end-effector of the robotic arm. The symbol S_2 is the stiffness safety coefficient.

In addition to the deformation constraints, the dynamic frequency of the robotic arm should be considered in the lightweight design. Thus, the natural frequency of the present robotic arm is constrained to attain better dynamic characteristics. In the optimization, the natural frequency is calculated in ABAQUS and need meet the following conditions:

$$\begin{aligned}
v (\mathbf{X}) &\geq \mathbf{f}, \\
f &= \max\{n_j \big/ 60, j = 1, 2, 3, 4\},
\end{aligned} \tag{12}$$

where $v(\mathbf{X})$ is the first natural frequency (FF) of the robotic arm, and f is the maximum value of the excited frequencies from four joint speeds (n_j) of the robotic arm.

3) CONSTRAINTS ON BONDING DAMAGE

In the hybrid structures, the AA ear plates are bonded with the CFRP link by using the bonding adhesive. The interfacial behavior of adhesive layer is analyzed by using the CZM. The fracture initiation of the adhesive layer is evaluated by the quadratic stress criterion [34], which is widely applied in adhesive joint and described as:

$$\left[\frac{< \sigma_n (\mathbf{X}) >}{\sigma_{nc}}\right]^2 + \left[\frac{\sigma_s (\mathbf{X})}{\sigma_{sc}}\right]^2 + \left[\frac{\sigma_t (\mathbf{X})}{\sigma_{tc}}\right]^2 = 1, \tag{13}$$

where σ_n, σ_s, σ_t, and σ_{nc}, σ_{sc}, σ_{tc} denote the normal stress, in-plane shear stress, out-of-plane shear stress, and corresponding critical values, respectively. The mathematic symbol $<>$ represents the Macauley operator as: $< x >= 0.5(x + |x|)$.

When there is damage propagation in the adhesive layer, a damage parameter D, which is represented by the damage
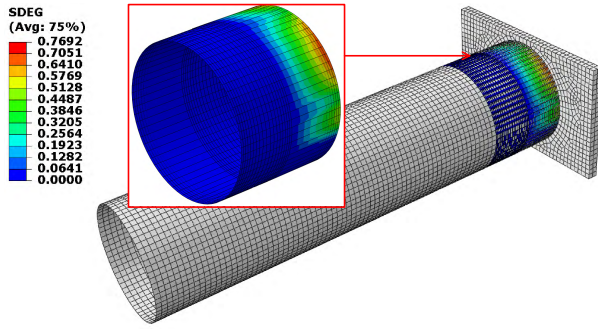
FIGURE 6. Simulation results of the adhesive layer in hybrid structure.

stiffness of cohesive elements, is described as:

$$D(\mathbf{X}) = \begin{cases} 0, & \delta_m \leq \delta_{m0}, \\ \dfrac{\delta_{m1}(\delta_m - \delta_{m0})}{\delta_m(\delta_{m1} - \delta_{m0})}, & \delta_{m0} < \delta_m < \delta_{m1} \\ 1, & \delta_m \geq \delta_{m1}, \end{cases} \quad (14)$$

where δ_m is an equivalent value of the strain in the adhesive layer, δ_{m0} and δ_{m1} are the corresponding values at the begin and end of fracture. The values 0 and 1 represent that the cohesive layer is perfect and complete fracture. Between the values 0 and 1, the strains and stresses can be described as:

$$\begin{bmatrix} \sigma_n \\ \sigma_s \\ \sigma_t \end{bmatrix} = \begin{bmatrix} (1-D)K_{nn} + \dfrac{<-\delta_n>}{-\delta_n} & 0 & 0 \\ 0 & (1-D)K_{ss} & 0 \\ 0 & 0 & (1-D)K_{tt} \end{bmatrix}$$
$$\times \begin{bmatrix} \delta_n \\ \delta_s \\ \delta_t \end{bmatrix}, \quad (15)$$

where K_{nn}, K_{ss} and K_{tt} represent the damage stiffness in normal and both tangential directions. δ_n, δ_s and δ_t represent the strains in normal and both tangential directions. The equivalent value of the strain is described as:

$$\delta_m = \sqrt{(<\delta_n>)^2 + (\delta_s)^2 + (\delta_t)^2}.$$

As a result, the constraints on bonding damage for adhesive zone are represented by:

$$D(\mathbf{X}) < D_f, \quad (16)$$

where D_f is the maximum value of permissible damage parameter with reliable connections.

In this study, the parameter D that is equal to the index SDEG is evaluated in the ABAQUS software. For example, a mesh model of adhesive layer in the second hybrid structure is presented with the value of SDEG as shown in Fig. 6. If the value of SDEG is less than 1, the adhesive layer is undamaged.

C. OBJECTIVE FUNCTION

In this study, the objective of the optimization problem is to design a lightweight robotic arm with CFRP/AA hybrid structures that fulfill all constraint conditions on strength, stiffness
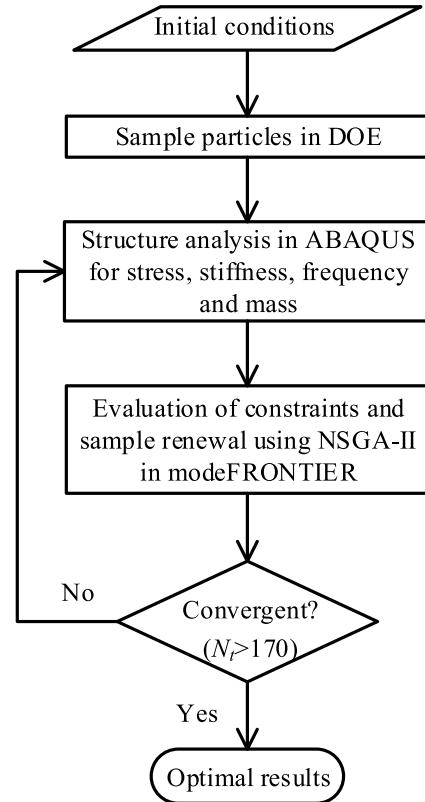

FIGURE 7. Flowchart of the hybrid structure optimization for the lightweight robotic arm.

and bonding damage. The objective function is defined as:

$$Mininizeh(X) = h_1(X_1) + h_2(X_2), \quad (17)$$

where $h_1(X_1)$ and $h_2(X_2)$ is the mass of the first and second hybrid structure respectively, and $h(X)$ denotes the total mass of hybrid structures.

D. DESIGN PROCESS AND ALGORITHM

Figure 7 depicts the flowchart of the hybrid structure optimization for the lightweight robotic arm, which consists of design of experiment (DOE), FEM analysis, data process and renewal.

First, the initial conditions are presented and the initial population (N_p) related to the design variables are generated by DOE, where each sample need fulfill all constraint conditions.

Second, the design variables of samples are imported into ABAQUS and the parameterized models of the robotic arms with hybrid structures are automatically established to calculate the values of stress, stiffness, frequency and mass of the hybrid structures by using a Python script language in ABAQUS. According to the condition in Eq. (6), CFRP links and CSJH are discretized into shell elements in FEM analysis. While the adhesive layers are calculated with cohesive elements and the other parts are modeled with

TABLE 3. Values of mechanical parameters of CFRP Material (unit: GPa).

Longitudinal Young's modulus, E_1	114
Transverse Young's modulus, $E_2(E_3)$	8.61
In-plane Shear modulus, $G_{12}(G_{13})$	4.16
Out-of-plane Shear modulus, G_{23}	3
In-plane Poisson's ratio, $v_{12}(v_{13})$	0.3
Out-of-plane Poisson's ratio, v_{23}	0.45
Longitudinal tensile strength, X_t	2.688
Longitudinal compressive strength, X_c	1.458
Transverse tensile strength, Y_t	0.0695
Transverse compressive strength, Y_c	0.236
In-plane shear strength, S	0.136

TABLE 4. Mapping relationship between numbers and ply angles.

Number	0	1	2	3
Ply angle (°)	-45	0	45	90

solid elements. In addition, the whole robotic arm is meshed with the size of 2.5 mm. The foundation bed of the robotic arm is fixed upon six degrees of freedom and the end effector is subjected to a given load.

Third, every calculated result of samples are evaluated with corresponding constraints to select the feasible individuals and produce new individuals, which are used to generate a new population by using NSGA-II in modeFRONTIER.

Finally, the second and third steps are calculated all over again until the iteration number of calculation N_t exceed the minimum iteration number a_t.

In conclusion, the whole optimization process is performed on integrated platform with Python script in ABAQUS used to static analysis and the genetic algorithm in modeFRONTIER. After the optimization, a dynamic analysis for the optimized robotic arm in MSC.ADAMS is conducted to validate the energy conversation and driving ability.

IV. DESIGN EXAMPLE

A. MATERIAL PARAMETERS AND CALCULATION CONDITIONS

To optimize the robotic arm, the material parameters are necessary to be specified. The robotic arm with hybrid structures is made of aluminum alloy (6061-T6) and carbon fiber (T700/BA9916), and the mechanical parameters of materials are assigned to evaluate the strength and stiffness. The aluminum alloy is an isotropic material, and its Young's modulus E_A and yield strength σ_s are assigned to 69000 Mpa and 270 MPa, respectively. While carbon fiber is anisotropic material, so the elasticity modulus and yield strength include various parameters and are listed in Table 3.

Regarding the bonding adhesive, the critical stress are set as $\sigma_{nc} = 60$ MPa, $\sigma_{sc} = \sigma_{tc} = 80$ MPa, the initial damage stiffness are given as $K_{nn} = 2$ GPa, $K_{ss} = K_{tt} = 1.5$ GPa, and the release rates of fracture energy are fixed as $G_n^C = 0.78$ N/mm, $G_s^C = G_t^C = 1.36$ N/mm, respectively. The damage parameter of cohesive zone is $D_f = 1$ mm.

In addition, the Poisson's ratio of aluminum alloy and bonding adhesive are fixed as 0.32 and 0.33 respectively, and the thickness t_c of prepreg is given as 0.2 mm. The density of aluminum alloy (ρ_A) and CFRP (ρ_c) materials are 2700 kg/m^3 and 1600 kg/m^3, respectively. The structural and

stiffness safety coefficients are set to $S_1 = S_2 = 1.2$, and the maximum value of allowable deformation in three directions is given as $d_a = 0.6$ mm. The maximum value of Tsai-Wu failure index C_{vmax} is set to 1.

In the genetic algorithm, the initial population N_p, which is generated in modeFRONTIER by DOE based on a random sequence, is given as 17 and the number of generation N_g is set to 10. Hence, the minimum iteration number a_t should be 170.

B. INITIALIZATION OF DESIGN VARIABLES

Besides the material parameters and calculation conditions, the initial values and feasible ranges of the design variables are necessary. In particular, the stacking sequences represented by a group of ply angles are transformed into an integer variable to facilitate the programmable computation and realize updating in optimization. The mapping relationship between ply angles and numbers is listed in Table 4. Based on the mapping relationship, the transformation formula of the stacking sequences into integer variables are represented by:

$$Seq_{Ji} = \sum_{j=1}^{N_{Ji}} 4^{N_{Ji}-j}\theta_j^i, \quad Seq_{Li} = \sum_{j=1}^{M_{Li}} 4^{M_{Li}-j}\beta_j^i,$$
$$\theta_j^i \in [0, 1, 2, 3], \quad \beta_j^i \in [0, 1, 2, 3], \tag{18}$$

Four ply angles are used in the transformation and then any stacking sequence can be transformed into a quaternary number, which is an integer to simplify the description and calculation.

In this design example, the initial values and ranges of the design variables of CFRP/AA hybrid structures are described and listed with data type and step-size as shown in Table 5. All the starting values in these ranges are the initial values of the corresponding design variables. And then, initial populations are produced to perform the genetic algorithm based on the initial values and ranges of design variables in modeFRONTIER.

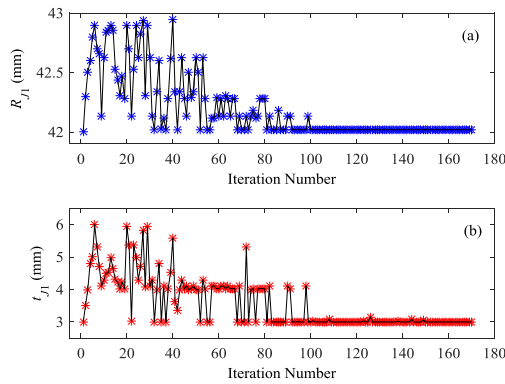### C. OPTIMAL RESULTS AND DISCUSSION

Based on these parameter values of materials used in the hybrid structures and initialization of design variables, the CFRP/AA hybrid structures in the robotic arm can be achieved optimum solution.

Figures 8 and 9 illustrate the convergences of the design variables of joint housing and link in the first hybrid structure. In the convergences, these values of design variables, which change within the given ranges and make the calculated results fulfill all conditions, are retained and marked in

TABLE 5. Initial values and ranges of design variables of hybrid structures.

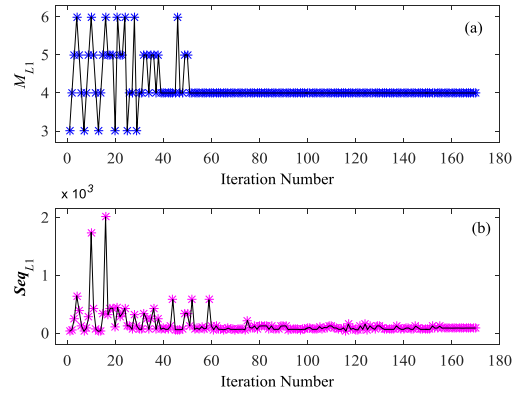| Object	Description of design variables	Data type	Range	Step-size
Hybrid structure 1	Layer number of link, M_{L1}	Integer	[3, 6]	1
	Stacking sequences of link, $\textbf{\textit{Seq}}_{L1}$		[0, 4096]	
	Layer number of CSJH, N_{J1}		[3, 7]	
	Stacking sequences of CSJH, $\textbf{\textit{Seq}}_{J1}$		[0, 16384]	
	Outside radius of ALJH, R_{J1} (unit: mm)	Float	[42, 43]	0.01
	Thickness of plated in ALJH, t_{J1} (unit: mm)		[3, 6]	0.1
Hybrid structure 2	Layer number of link, M_{L2}	Integer	[3,6]	1
	Stacking sequences of link, $\textbf{\textit{Seq}}_{L2}$		[0, 4096]	
	Layer number of CSJH, N_{J2}		[3, 6]	
	Stacking sequences of CSJH, $\textbf{\textit{Seq}}_{J2}$		[0, 4096]	
	Outside radius of ALJH, R_{J2} (unit: mm)	Float	[39, 40]	0.01
	Thickness of plated in ALJH, t_{J2} (unit: mm)		[3, 6]	0.1

FIGURE 8. Convergences of design variables of joint housing in the first hybrid structure: (a) R_{J1} and (b) t_{J1}.

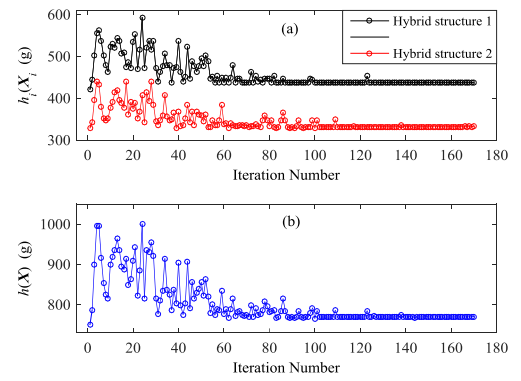**TABLE 6.** Optimal results of all design variables of the both hybrid structures.

Index i	R_{Ji} (mm)	t_{Ji} (mm)	N_{Ji}	$\textbf{\textit{Seq}}_{Ji}$	M_{Li}	$\textbf{\textit{Seq}}_{Li}$
1	42.02	3	5(10)	584	4(8)	179
2	39.07	3	3(6)	60	4(8)	125

FIGURE 9. Convergences of design variables of CFRP link in the first hybrid structure: (a) M_{L1} and (b) $\textbf{\textit{Seq}}_{L1}$.

FIGURE 10. Convergences of weight of the hybrid structures: (a) $h_i(X_i)$ and (b) $h(X)$.

FIGURE 11. Experimental prototype of the both hybrid structures.

color points. The design variables R_{J1} and t_{J1} of ALJH are convergent to the optimal results that are close to the smallest values in the given ranges through about 100 iterations. The other design variables can converge faster except that the design variable N_{J1} converges to a stable value in the need of 123 iterations.

Table 6 presents the optimal results of the design variables of both hybrid structures. It can be observed that the stacking sequences of all CFRP parts are solved in integers, which can be transformed into quaternary sequences by means of

Eq. (18). Therefore, the stacking sequences represented by quaternary sequences can be mapped to the ply angles in terms of the mapping relationship shown in Table 4. As a result, the optimal results of the design variables $\textbf{\textit{Seq}}_{J1}$, $\textbf{\textit{Seq}}_{J2}$, $\textbf{\textit{Seq}}_{L1}$ and $\textbf{\textit{Seq}}_{L2}$ listed in Table 6 are transformed into the angular vectors [−45° /90° /−45° /0° /0°], [−45° /90° /-45°], [90° /0/90° /0] and [0/ 90° /90° /0], respectively.

In addition, the actual ply numbers are double the optimal results of the design variables N_{Ji} and M_{Li}, and are represented by the numbers in brackets in Table 6. The ply orientations of CFRP parts are designed symmetrically, so the actual stacking sequences are described as [−45° /90° /−45°

FIGURE 12. (a) Experimental prototype of the lightweight CFRP/AA arm, (b) Experimental prototype of the lightweight AA arm, (c) EPOS-studio in PC, and (d) schematic of torque measurement.

TABLE 7. Optimal results of mass of the hybrid structure in robotic arms (unit: g).

Object	Hybrid structure	AA structure [31]	Reduction rate (%)
$h_1(X_1)$	437.35	605.67	27.84%
$h_2(X_2)$	332.31	411.32	19.21%
$h(X)$	769.66	1016.99	24.32%

/0° /0°$]_s$, $[-45°$ /90° /-45°$]_s$, [90° /0/90° /0]$_s$ and [0/90° /90° / 0]$_s$, respectively.

Figure 10 depicts the convergences of the weight of hybrid structures. In Figure 10(a), the symbol $h_i(X_i)$ denotes the mass of the *i*th hybrid structure. The convergence of the weight of the second hybrid structure is faster than that of the first hybrid structure because the second hybrid structure is a load on the first hybrid structure and the former can affect the latter, which is not completely dependent on the former in calculation. Figure 10(b) shows the convergence of the total weight of hybrid structures in the robotic arm. The optimal results of the mass of hybrid structures are listed in Table 7, and are compared with the corresponding values of the counterpart in the AA prototype.

Table 7 shows that the hybrid structure design has a reduction of 27.84% and 19.21% of the mass of monolithic hybrid structure respectively, by comparing with the AA structure design [31]. These results imply that the first hybrid structure has larger optimized space than the second hybrid structure. As a result, the total mass of hybrid structures has a reduction of 24.32%, which is in between the values of 27.84% and 19.21%, in comparison with the mass of AA structures. Hence, the hybrid structure design of the robotic arm can obtain a lighter structure, and a series of experiment tests are performed on the prototype to validate the hybrid structure design.

V. EXPERIMENT AND VERIFICATION
A. EXPERIMENTAL PROTOTYPE AND TRAJECTORIES
Figure 11 depicts the experimental prototypes of the both hybrid structures, which are made of T700/BA9916 and 6016-T6 based on the optimal results. The total mass of the experiment prototypes of the hybrid structure have a

reduction of 21.37%, in comparison with the total mass of the prototypes of the AA structure. The result is close to the abovementioned theoretical result 24.32% and show that the hybrid structure design is relatively accurate.

To verify the validity of the optimization and the energy-saving objective of the lightweight robotic arm, the robot prototype with hybrid structures is made to compare with that of the robot prototype made of AA structures.

In the comparison of dynamic characteristics, the trajectories are necessary for calculation and measurement of the torque. The robotic arm is conducted in four motions, which result from two types of installations and two motions for each installation. In the measurement and calculation, the maximum required torque of the joint 1 occurs in the case of wall installation, while the maximum required torques of joints 2–4 occur in the case of ground installation. In addition to the positions of trajectories listed in Table 2, the velocities and accelerations of trajectories at starting and ending times are assumed as zero for smooth motions.

B. EXPERIMENTAL RESULTS ON TORQUES
Based on the prototype of hybrid structures and other parts used in the AA robotic arm, we can build an experimental prototype of the lightweight robotic arm with hybrid structures. Figure 12 shows the two versions experimental prototypes, which perform the same control action for comparison, and the measurement scheme of torques using the EPOS-studio in PC. The torque values of joints are obtained by transforming the current data, which are exported from the drivers of the motors by using USB cables. The transformation formula is represented by:

$$\tau_i(t) = K_{Ti}I_{mi}(t)i_g\eta, \quad i = 1, 2, 3, 4, \quad (19)$$

where η and i_g are the average efficiency and reduction ratio respectively, while $I_{mi}(t)$ and K_{Ti} are the measured current values and torque constant respectively. And $\tau_i(t)$ represents the torque of the *i*th joint.

The torque constants of the four Maxon motors used in the drivetrains are $K_{T1} = K_{T2} = 91$ mN·m/A, $K_{T3} = 30.5$ mN·m/A, and $K_{T4} = 36.9$ mN·m/A. In this analysis, the average efficiency η and reduction ratio i_g of drivetrains
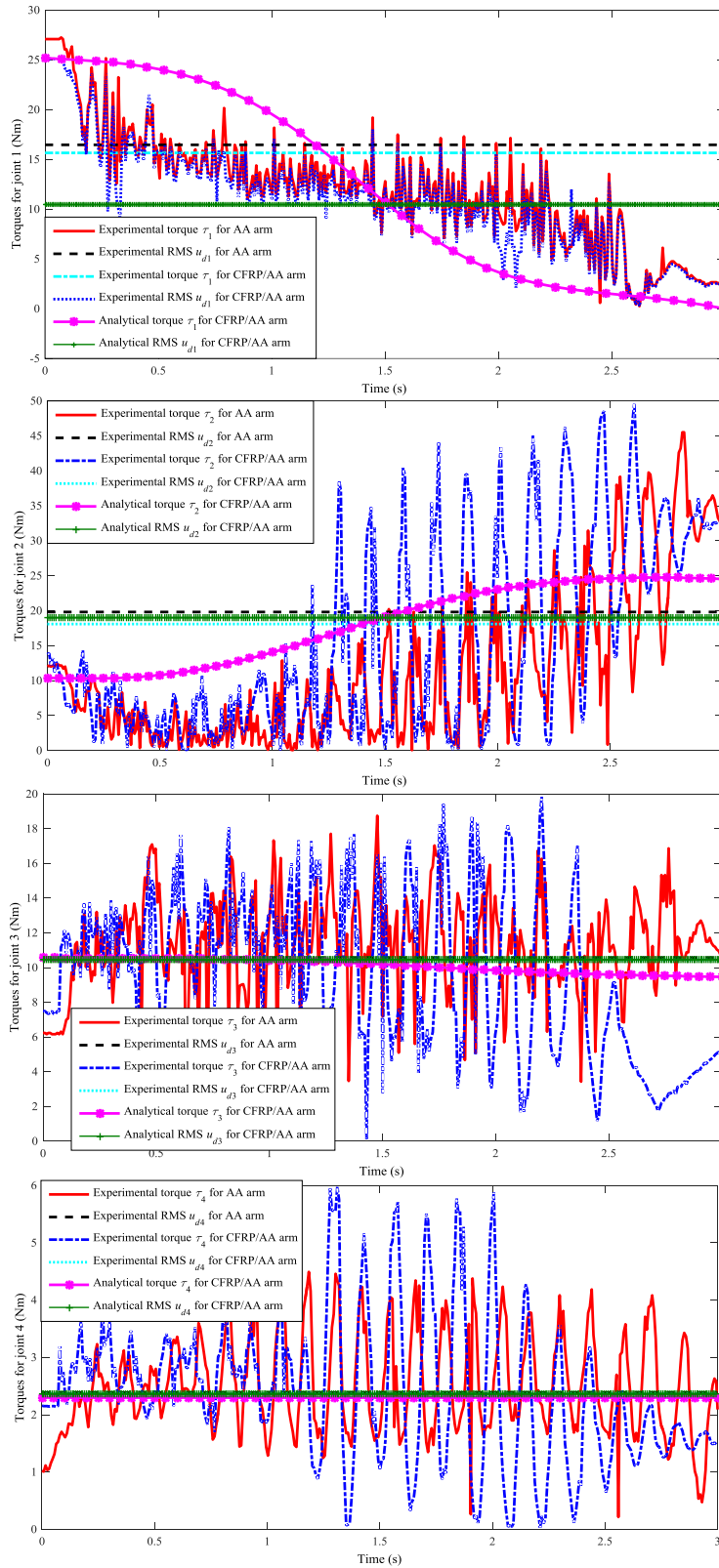
FIGURE 13. Experimental and theoretical results of torques for four joints.

are used as 0.76 and 120 according to the data from catalog of motors and gears. The measured current values and its root mean square (RMS) are transformed into experimental

torques (τ) and the corresponding RMS (u_d) for CFRP/AA arm (blue lines) as shown in Fig. 13. In the measurement, the experimental prototype tracks the same trajectories as the

TABLE 8. Experimental RMS Of torques for the both versions prototypes and comparison results (uint: N·m).

Joint index	RMS of torques		Reduction
	CFRP/AA arm	AA arm	
1	15.65	16.48	5.3%
2	18.09	19.12	5.7%
3	10.45	10.57	1.1%
4	2.37	2.38	0.4%

simulation, and the RMS of measured torques are 15.65 N·m, 18.09 N·m, 10.45 N·m, and 2.37 N·m, respectively, which are used to compare with the analytical results. Figure 13 also depicts the analytical torques and their RMS for CFRP/AA arm (pink and green lines) in simulation, and the RMS of calculated torques are 15.31 N·m, 19.02 N·m, 10.11 N·m, and 2.299 N·m, respectively. It is observed that the errors between the analytical and experimental RMS of torques are −2.22%, 4.89%, −3.36%, and −3.09%, respectively. The absolute values of errors are less than 5% and imply that the calculation and optimization of the lightweight robotic arm are relatively accurate.
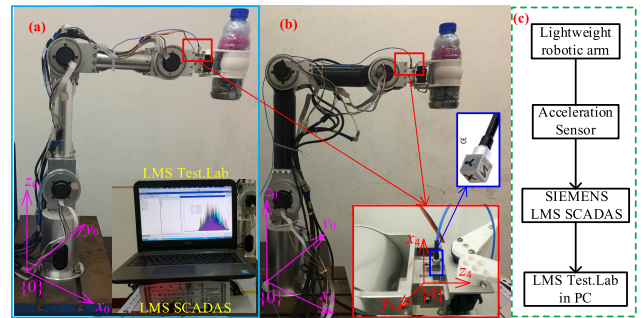
All the theoretical and experimental RMS of torques are less than the rated values of the selected components, which are 21.342 Nm, 21.342 Nm, 11.674 Nm, and 2.462 Nm as illustrated in Table 1. The comparisons imply that the design method is valid and the experimental prototype is safe.

Moreover, the experimental RMS of torques of the CFRP/AA prototype are compared with that of the AA prototype, which are also depicted as black lines in Fig. 13. Table 8 lists the experimental values of the both prototypes and comparison results. The experimental RMS of all joints torques of the CFRP/AA prototype are less than the corresponding value of the AA prototype, and the CFRP/AA prototype has a reduction of 5.4%, 5.7%, 1.1%, and 0.4% of experimental RMS for four joints, respectively. As a result, the optimal prototype with CFRP/AA hybrid structures can provide the operation with lower energy-consumption than the optimal prototype with AA structures under the action of the same working tasks.
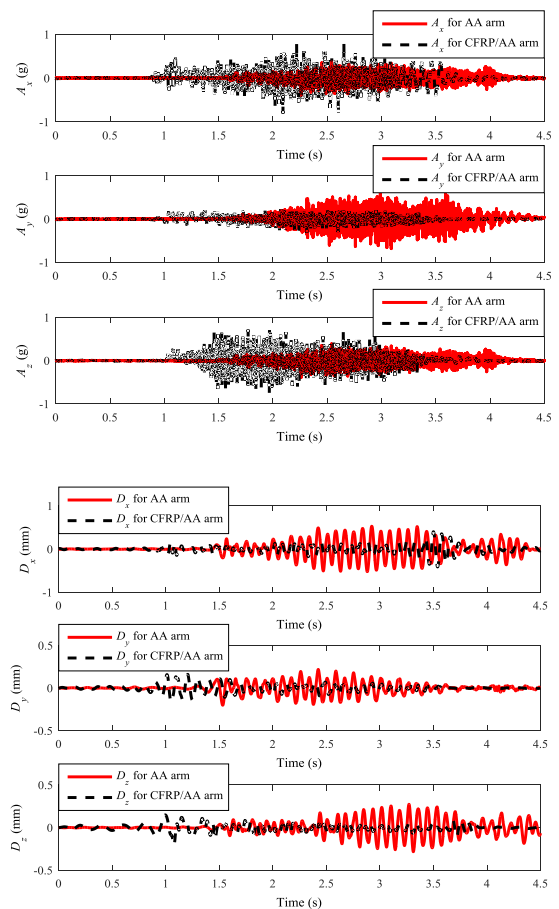
1) EXPERIMENTAL RESULTS ON STIFFNESS CONDITIONS
In addition, the lightweight design makes the robotic arm become flexible, thus, the stiffness of the designed robotic arms are necessary to check. To validate the stiffness conditions in the design of robotic arms, a series of experiments on modal frequency and deflection measurement are achieved.

The lightweight design results in large deformation of the robotic arm at end-effector. So the deflections at the end-effectors of the both versions robotic arms are measured by using the ICP accelerometer (356A03) and data-acquisition instrument (SEMENS LMS SCADAS) shown in Fig. 14(a) and (b). The measuring schematic is shown in Fig. 14(c) and the measured accelerations are transformed into displacements through the LMS Test. Lab.

FIGURE 14. Experimental prototypes with accelerometer for (a) AA arm, (b) CFRP/AA arm, and (c) schematic of deflection measurement.

FIGURE 15. Accelerations (*A*) and displacements (*D*) of deflections for two versions arms in local frame {4}.

Figure 15(a) shows the accelerations of deflections for the both versions robotic arms in local coordinate frame {4}, which can be transformed into local displacements shown in Fig. 15(b) by integral calculation. The local displacements of deflections are transformed into the corresponding global values by using the following formula:

$$^0\boldsymbol{D} =^0 \boldsymbol{T}_4(\boldsymbol{q})^4\boldsymbol{D} \tag{20}$$

where $^0\boldsymbol{D} = [^0D_x, ^0D_y, ^0D_z]$ and $^4\boldsymbol{D} = [^4D_x, ^4D_y, ^4D_z]$ are the global and local displacements of deflections,

TABLE 9. Maximum global displacements of deflections for the both CFRP/AA and AA prototypes.

Prototypes	Displacements (unit: mm)		
	x_0 direction	y_0 direction	z_0 direction
AA	0.2683	0.1514	0.5287
CFRP/AA	0.1717	0.1968	0.4123

TABLE 10. Modal frequencies of CFRP/AA and AA prototypes (unit: Hz).

Model	First frequency	Increase
CFRP/AA prototype	19.88	10.26%
AA prototype	18.03	

respectively, $^0T_4$ is the homogeneous transformation matrix, and q is the vector of the joint trajectory.

The maximum displacements of deflections in the global coordinate frame {0} for the both CFRP/AA and AA robotic arms are obtained and listed in Table 9. All the displacements of deflections in three directions are less than the allowable value of deformation $d_a = 0.6$ mm used in the optimization. The results imply that the designed lightweight robotic arm meets the stiffness requirements. Moreover, the maximum vibrations displacements appear in z_0 direction, the result reflect the influence of load. The CFRP/AA robotic arm has a reduction of 22% of the maximum vibration displacement in z_o direction by comparing with the AA robotic arm. The results imply that the CFRP/AA robotic arm possess larger stiffness and higher positioning accuracy than the AA robotic arm.

In addition, based on these data of vibration displacement in z_o direction, the frequency-domain spectra of the robot prototypes are obtained by fast Fourier transformation (FFT). The first frequencies of the CFRP/AA prototype and the AA prototype are listed in Table 10, and the first frequency of the CFRP/AA prototype increase 10.26% than that of the AA prototype. As a result, the CFRP/AA robotic arm can provide lower amplitude of vibration and higher natural frequency than the AA prototype.

VI. CONCLUSIONS

A hybrid structure design was proposed to optimize lightweight robotic arms. In this method, the CFRP and AA materials were used to build composite components, which replace the upper arm and forearm in the previously designed AA robotic arm. The CFRP and AA material modules were simultaneously optimized to obtain the optimal configuration under specific structure strength and dynamic performance constraints by using NSGA-II algorithm. Thus, the hybrid structure design has a reduction of 24.32% of the total mass of the both arms by comparing with the AA structure design.

On the basis of the optimal results, the robotic arm with hybrid structure prototype was built and three experiments

on joint torques, deflections and frequency of the designed robotic arm were implemented to validate the optimization. Comparing with that of the AA prototype, the maximum reduction rate of joint torque was 5.7%, the vibration displacements of deflections at end-effector reduced 22% and the first natural frequency of the CFRP/AA prototype increased up to 19.88 Hz. Those analysis results imply that the robotic arm with hybrid structures can provide lower energy consumption, higher motion precision, and better dynamic performance than the AA prototype.

The hybrid structure design can improve lightweight and energy saving level, and dynamic performance for the robotic arms, which are used in service industry. However, the design variables of stacking sequences were searched in limited values, therefore, the winding process and its reliability in joint housing due to the heat influence from drivetrains will be part of our further research.

REFERENCES

[1] B. Tondu, S. Ippolito, J. Guiochet, and A. Daidie, "A seven-degrees-of-freedom robot-arm driven by pneumatic artificial muscles for humanoid robots," *Int. J. Robot. Res.*, vol. 24, no. 4, pp. 257–274, 2005.

[2] T. N. Do, T. Tjahjowidodo, M. W. S. Lau, T. Yamamoto, and S. J. Phee, "Hysteresis modeling and position control of tendon-sheath mechanism in flexible endoscopic systems," *Mechatronics*, vol. 24, no. 1, pp. 12–22, 2014.

[3] H. Fang, C. Wang, S. Li, K. W. Wang, and J. Xu, "A comprehensive study on the locomotion characteristics of a metameric earthworm-like robot," *Multibody Syst. Dyn.*, vol. 35, no. 2, pp. 153–177, 2015.

[4] Y. Fujishima, S. Wakao, A. Yamashita, and T. Katsuta, "Design optimization of a permanent magnet synchronous motor by the response surface methodology," *J. Appl. Phys.*, vol. 91, no. 10, pp. 8305–8307, 2002.

[5] S. Jing, Z. Hongwei, and L. Yongping, "Structure optimization for brushless DC motor in robot's arms using FEM," in *Proc. Int. Conf. Electr. Mach. Syst.*, Oct. 2007, pp. 699–702.

[6] E. Sulaiman, T. Kosaka, and N. Matsui, "Design and analysis of high-power/high-torque density dual excitation switched-flux machine for traction drive in HEVs," *Renew. Sustain. Energy Rev.*, vol. 34, pp. 517–524, Jun. 2014.

[7] M. Pettersson and J. Ölvander, "Drive train optimization for industrial robots," *IEEE Trans. Robot.*, vol. 25, no. 6, pp. 1419–1424, Dec. 2009.

[8] L. Zhou, S. Bai, and M. R. Hansen, "Integrated dimensional and drive-train design optimization of a light-weight anthropomorphic arm," *Robot. Auton. Syst.*, vol. 60, no. 1, pp. 113–122, Jan. 2012.

[9] P. S. Shiakolas, D. Koladiya, and J. Kebrle, "Optimum robot design based on task specifications using evolutionary techniques and kinematic, dynamic, and structural constraints," *Inverse Problems Eng.*, vol. 10, no. 4, pp. 359–375, 2002.

[10] B. J. Kim, D. K. Yun, S. H. Lee, and G. W. Jang, "Topology optimization of industrial robots for system-level stiffness maximization by using part-level metamodels," *Struct. Multidisciplinary Optim.*, vol. 54, no. 4, pp. 1061–1071, Oct. 2016.

[11] A. Gasparetto, A. K. Moosavi, P. Boscariol, and M. Giovagnoni, "Experimental validation of a dynamic model for lightweight robots," *Int. J. Adv. Robotic Syst.*, vol. 10, no. 3, p. 182, 2013.

[12] X. Yang, S. S. Ge, and W. He, "Dynamic modelling and adaptive robust tracking control of a space robot with two-link flexible manipulators under unknown disturbances," *Int. J. Control*, vol. 91, no. 4, pp. 969–988, 2018.

[13] I. M. Fonseca and P. M. Bainum, "Integrated structural and control optimization," *J. Vib. Control*, vol. 10, no. 10, pp. 1377–1391, 2004.

[14] D. Lee, T. W. Seo, and J. Kim, "Optimal design and workspace analysis of a mobile welding robot with a 3P3R serial manipulator," *Robot. Auton. Syst.*, vol. 59, no. 10, pp. 813–826, Oct. 2011.

[15] F. Cheng, R. Yin, Y. Zhang, C.-C. Yen, and Y. Yu, "Fully plastic micro-robots which manipulate objects using only visible light," *Soft Matter*, vol. 6, no. 15, pp. 3447–3449, 2010.

[16] M. Shibata and N. Sakagami, "Fabrication of a fish-like underwater robot with flexible plastic film body," *Adv. Robot.*, vol. 29, no. 1, pp. 103–113, 2015.

[17] H. Hagenah, W. Böhm, T. Breitsprecher, M. Merklein, and S. Wartzack, "Modelling, construction and manufacture of a lightweight robot arm," in *Proc. 8th Conf. Intell. Comput. Manuf. Eng.*, 2012, pp. 211–216.

[18] E. Baumeister and S. Klaeger, "Advanced new lightweight materials: Hollow-sphere composites (HSCs) for mechanical engineering applications," *Adv. Eng. Mater.*, vol. 5, no. 9, pp. 673–677, Sep. 2003.

[19] E. Baumeister, S. Klaeger, and A. Kaldos, "Lightweight, hollow-sphere-composite (HSC) materials for mechanical engineering applications," *J. Mater. Process. Technol.*, vols. 155–156, pp. 1839–1846, Nov. 2004.

[20] P. M. Kebria, S. Al-wais, H. Abdi, and S. Nahavandi, "Kinematic and dynamic modelling of UR5 manipulator," in *Proc. IEEE Int. Conf. Syst., Man, Cybern.*, Oct. 2016, pp. 4229–4234.

[21] S. Shepherd and A. Buchstab, "KUKA robots on-site," in *Robotic Fabrication in Architecture, Art and Design*. Cham, Switzerland: Springer, 2014, pp. 373–380.

[22] D. X. Liao, C. K. Sung, and B. S. Thompson, "The design of flexible robotic manipulators with optimal arm geometries fabricated from composite laminates with optimal material properties," *Int. J. Robot. Res.*, vol. 6, pp. 116–130, 1987.

[23] C. S. Lee, D. G. Lee, J. H. Oh, and H. S. Kim, "Composite wrist blocks for double arm type robots for handling large LCD glass panels," *Compos. Struct.*, vol. 57, nos. 1–4, pp. 345–355, Jul. 2002.

[24] S.-Y. Yoo, B.-H. Jun, H. Shim, and P.-M. Lee, "Design and analysis of carbon fiber reinforced plastic body frame for multi-legged subsea walking robot, crabster," *Ocean Eng.*, vol. 102, pp. 78–86, Jul. 2015.

[25] S. A. Mutasher, B. B. Sahari, A. M. S. Hamouda, and S. M. Sapuan, "Experimental study of bending fatigue characteristics of a hybrid aluminum/composite drive shaft," *J. Compos. Mater.*, vol. 41, no. 18, pp. 2267–2288, 2007.

[26] P. Feng, L. Hu, P. Qian, and L. Ye, "Compressive bearing capacity of CFRP–aluminum alloy hybrid tubes," *Compos. Struct.*, vol. 140, pp. 749–757, Apr. 2016.

[27] D. K. Shin, H. C. Kim, and J. J. Lee, "Numerical analysis of the damage behavior of an aluminum/CFRP hybrid beam under three point bending," *Compos. B, Eng.*, vol. 56, pp. 397–407, 2014.

[28] T. E. A. Ribeiro, R. D. S. G. Campilho, L. F. M. D. Silva, and L. Goglio, "Damage analysis of composite–aluminium adhesively-bonded single-lap joints," *Compos. Struct.*, vol. 136, pp. 25–33, Feb. 2016.

[29] S.-W. Jeon, Y. H. Cho, M.-G. Han, and S.-H. Chang, "Design of carbon/epoxy–aluminum hybrid upper arm of the pantograph of high-speed trains using adhesive bonding technique," *Compos. Struct.*, vol. 152, pp. 538–545, Sep. 2016.

[30] T. M. Hemmerling, R. Taddei, M. Wehbe, C. Zaouter, S. Cyr, and J. Morse, "First robotic tracheal intubations in humans using the kepler intubation system," *Brit. J. Anaesthesia*, vol. 108, no. 6, pp. 1011–1016, Jun. 2012.

[31] H. Yin, S. Huang, M. He, and J. Li, "A unified design for lightweight robotic arms based on unified description of structure and drive trains," *Int. J. Adv. Robot. Syst.*, vol. 14, no. 4, pp. 1–14, 2017.

[32] G. Yang and I. M. Chen, "Equivolumetric partition of solid spheres with applications to orientation workspace analysis of robot manipulators," *IEEE Trans. Robot.*, vol. 22, no. 5, pp. 869–879, Oct. 2006.

[33] M. Akbulut and F. O. Sonmez, "Design optimization of laminated composites using a new variant of simulated annealing," *Comput. Struct.*, vol. 89, nos. 17–18, pp. 1712–1724, 2011.

[34] M. F. S. F. De Moura, J. P. M. Gonçalves, J. A. G. Chousal, and R. D. S. G. Campilho, "Cohesive and continuum mixed-mode damage models applied to the simulation of the mechanical behaviour of bonded joints," *Int. J. Adhes. Adhesives*, vol. 28, pp. 419–426, Dec. 2008.

HAIBIN YIN received the B.Eng. and M.Eng. degrees from the University of Science and Technology Beijing (USTB), in 2002 and 2008, respectively, and the Ph.D. degree in human mechanical system and design from Hokkaido University (HU), Japan, in 2011. He is currently an Associate Professor with the School of Mechanical and Electronic Engineering, Wuhan University of Technology (WHUT), China. His research interests include the dynamic design of robots, flexible robots, and soft robots.

JING LIU received the B.Eng. degree in mechanical engineering and automation from Huaqiao University, China, in 2017. He is currently pursuing the master's degree with the School of Mechanical and Electronic Engineering, Wuhan University of Technology, China. His main research interests include the lightweight design and control of robots.

FENG YANG received the B.Eng. degree in mechanical engineering from Wuhan Textile University, China, in 2015, and the M.Eng. degree in mechanical and electronic engineering from the Wuhan University of Technology, China, in 2018. His main research interests include the lightweight design and control of robotic arms.

● ● ●